Icarus 219 (2012) 194–210

Contents lists available at SciVerse ScienceDirect

Icarus

journal homepage: www.elsevier.com/locate/icarus

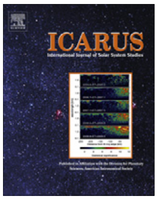

First microwave map of the Moon with Chang'E-1 data: The role of local time in global imaging

Y.C. Zheng [a,b,*], K.T. Tsang [b], K.L. Chan [b], Y.L. Zou [a], F. Zhang [a], Z.Y. Ouyang [a,c]

[a] National Astronomical Observatories, Chinese Academy of Sciences, Beijing 100012, China
[b] Centre for Space Science Research, Hong Kong University of Science and Technology, Hong Kong
[c] Institute of Geochemistry, Chinese Academy of Sciences, Guiyang 550002, China

ARTICLE INFO

Article history:
Received 30 March 2011
Revised 30 January 2012
Accepted 14 February 2012
Available online 1 March 2012

Keywords:
Radio observations
Regoliths
Moon, Surface

ABSTRACT

Among recent lunar orbiters, only the Chinese Chang'E-1 (CE-1) was equipped with a passive microwave radiometer (MRM) to measure the natural microwave emission from the lunar surface. The microwave emission, characterized by a frequency-dependent brightness temperature (TB), is related to the physical temperature and dielectric properties of the lunar surface. By measuring the brightness temperature at different frequencies, detailed thermal behavior and properties of the lunar surface can be retrieved. Using CE-1's microwave data, we present here a set of microwave maps of the Moon constructed through a rescaling of TB to noontime or midnight. The adopted processing technique helps to reduce the effect of mixing up the temporal and spatial variations introduced by the satellite's localized measurements which cover different locations of the globe at different lunar *local times*. The resulting maps show fine structures unseen in previous microwave maps that disregarded the local time effect. We discussed the new features revealed and their possible connections with the lunar geology.

1. Introduction

The eight scientific instruments on board the spacecraft Chang'E-1 (CE-1), China's first lunar orbiter, have delivered much new data during the mission (Ouyang et al., 2010). For example: the CCD stereo camera has produced a global image of the Moon with state-of-the-art quality and precision (Li et al., 2010); the Solar Wind Ion Detectors have discovered the acceleration of scattered solar wind protons close to the lunar polar terminator (Wang et al., 2010). Here we report on another scientific achievement of CE-1: the microwave radiometer (MRM) made it possible, for the first time, to globally map the Moon in microwave frequencies with unmatched spatial resolution and temperature sensitivity.

Passive microwave observation can sense emission from below the lunar surface (possibly down to 10 m, depending on the dielectric properties of the lunar regolith), and is able to "see" the permanently shadow region in the poles and the Moon at night regardless of solar illumination. Ground-based microwave measurements of the Moon have been studied at wavelengths of 1–500 cm since 1960s (Battaglia, 2003; Hirth et al., 1976; Keihm and Gary, 1979; Morabito et al., 2008; Schloerb et al., 1976). However, such observations have a number of drawbacks as: (i) they cannot observe the far side of the Moon; (ii) the spatial resolution is much lower than what can be done by a lunar satellite; and (iii) due to the presence of limb effects, interpretation of off-center data are much more difficult.

TB of the Moon and its characteristics were investigated theoretically and predicted by a number of authors (Fa and Jin, 2007a; Gary and Keihm, 1978; Hagfors, 1971; Keihm, 1982; Keihm and Gary, 1979; Muhleman, 1972). Interpretations of ground-based lunar microwave measurements were done based on different lunar regolith models (Feng et al., 2010; Keihm and Cutts, 1981; Schloerb et al., 1976). Passive orbital microwave measurements at different frequencies were proposed since the 1980s (Keihm, 1984), with the expectation that they could lead to the knowledge of global lunar heat flow and average regolith thickness. This thermal information, which is not available through active radar images of the Moon obtained by recent lunar orbiters Kaguya (Ono et al., 2009) and Chandrayaan-1 (Spudis et al., 2010), could provide important clues to understand the thermal evolution of the Moon and provide reliable estimation of valuable lunar resources, such as helium-3, due to their dependence on the thickness of regolith (Fa and Jin, 2007b).

CE-1's MRM TB data is widely recognized as the first, and currently the only set of data obtained from passive, multi-channel microwave sensor in lunar orbit. In this work we will present a detailed analysis of the MRM TB data and the global TB map resulting from such effort. The distinction between the work reported here and previous efforts (Fa and Jin, 2010; Wang et al., 2010a; Zhou

---

[*] Corresponding author at: National Astronomical Observatories, Chinese Academy of Sciences, Beijing 100012, China.

E-mail addresses: zyc@nao.cas.cn, mayczheng@ust.hk (Y.C. Zheng).

0019-1035/$ - see front matter Crown Copyright © 2012 Published by Elsevier Inc. All rights reserved.
doi:10.1016/j.icarus.2012.02.017

et al., 2010) is our emphasis on rigorous and comprehensive treatment of the lunar local time dependence. Since solar radiation is the dominant energy source on the lunar surface, and solar power received per unit area at a local spot depends on the angular separation between the Sun and the zenith, therefore lunar local time expressed in terms of an "hour angle" becomes the major driver of the diurnal TB variation, similar to the diurnal temperature variation on Earth. However, unlike the Earth, there is not much of seasonal temperature effect on the Moon due to the slightly tilted lunar rotation axis (by just 1.54°, much less than the 23.44° of the Earth) away from the normal of the Earth's orbital plane around the Sun. The "hour angle" introduced here roughly measures the angular distance between the local longitude and the lunar terminator. It is also related to the lunar phase cycle as observed on Earth, with the full Moon corresponding to local noon at the center of the nearside lunar disk. The use of solar hour angle as a local time measurement was introduced without much elaboration in our previous publication (Chan et al., 2010). In Section 3, this will be discussed in more detailed.

This paper is organized as following. In Section 2, a brief description of important aspects of the instrument and the data it acquired, which are relevant to our work, is given. In Section 3, a detailed discussion is provided to introduce the solar hour angle as an independent variable to characterize the lunar local time instead of the solar incident and azimuth angles used in the original study of MRM data. The mean relationship between TB and the solar hour angle at different latitudes could be modeled by a numerically fitted scheme so that the value of TB at any local time and latitude can be interpolated. In Section 4, the results of our GIS imaging technique are given in a series of TB maps. The merit of taking account of the solar hour angle effects is demonstrated by an example comparing our result – with the result from an earlier work which ignored such effects in composing the TB map. In Section 5, the hottest and coldest regions as revealed by the TB maps are located – and discussed. The correlation between TB and the composition (TiO_2 abundance) of surface materials were numerically analyzed and discussed. Finally, conclusion of this work is stated in Section 6.

2. Instrument and TB data sets

2.1. Instrument and calibration

CE-1, China's first scientific mission to explore planetary bodies beyond the Earth, was launched on 24th, October 2007. One set of microwave radiometers with four frequency channels, 3, 7.8, 19.35, and 37 GHz, was onboard to measure microwave emission from the Moon (Zheng et al., 2008). Except for the European Student Moon Orbiter (ESMO) (Montopoli et al., 2011) scheduled to be launched in late 2013 or early 2014, we are not aware of any planned future mission with a comparable program in passive microwave measurement of the Moon.

It took CE-1 13 days 14 h and 19 min to travel from the Earth to the Moon. The MRM was powered off during the early phases of CE-1's long journey. The MRM was then powered on and began taking TB measurements of the Moon after completing the first circumlunar orbit.

Since detail study on data calibration and data quality is not the purpose of this work, the interested readers are referred to the relevant literatures cited below. Here we briefly cover the issues involved for the sake of completeness and to provide readers with necessary backgrounds for our work. The CE-1 MRM was calibrated onboard periodically to assure its reliability and accuracy, using a two-point calibration method (Wang et al., 2010b; Zhang et al., 2008). A matching calibrating heat source of known temperature onboard provided the high temperature reference point, and the cold/deep space cosmic microwave background served as the low temperature reference point. Judging from the quality of TB maps produced from the data, we may conclude that the instrument was functioning as expected during most of its life-span in orbit (except possibly the 7.7 GHz channel; see later discussion) (Wang et al., 2010b; Zhang et al., 2008) brought to us reasonable results. As shown in the schematic view of the CE-1 MRM (Fig. 1), the four antennas at the left-side were designed to point to the cold/deep space which acted as the low temperature (2.7 K) calibrating source. The downward facing antennas were designed to point to the lunar surface for taking measurements. The sizes of the antenna dishes are proportional to the wavelengths of the four microwave channels.

As CE-1 had a circular polar orbit of 200 km above the lunar surface, MRM observations can achieve complete coverage with a nadir view. The spatial resolution is orders of magnitude better than any ground-based microwave observation. The sensitivity (0.5 K) and dynamical range (20–500 K) of observable TB is unsurpassed (Table 1). Due to the long lifespan of CE-1 (494 days), the MRM obtained eight sets of global TB data spanning full lunar day and night periods. The global, diurnal coverage of the TB data provides extremely valuable information for studying the physical properties of lunar regolith and thermal environment of the lunar surface.

2.2. Preprocessing flow of MRM data

Raw data acquired by the two ground stations, located in Miyun county in North China and Kunming city in Southwest China, were preprocessed at the Ground Receiving & Application System (GRAS) of China's Lunar Exploration Program (CLEP), located at National Astronomical Observatories, Chinese Academy of Sciences (Zheng et al., 2008). The data preprocessing flow was described in Table 2.

2.3. Elimination of peculiar data

Our work in this paper is based on the MRM level 2C data set, which has been distributed in the Chinese scientific community since June, 2008, and is now publicly available on the website: http://moon.bao.ac.cn. The level 2C data are stored in PDS format. Measurements in each individual track are stored in a single file. Each file contains a header and a table of measured data. The header provides the background data information and describes the meaning of every table column.

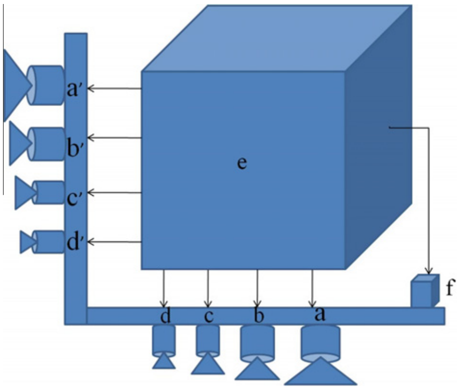

Fig. 1. Schematic view of the MRM onboard CE-1. (a′–d′) Cold space calibration antenna, (a–d) observation antenna, (e) microwave receiver, and (f) hot matching load on the instrument. MRM has two calibration modes and one observation mode, and switches between the calibration modes and observation mode periodically.

Table 1
Major technical specifications of CE-1 microwave radiometer.

Frequencies (GHz)	3.0 (±1%)	7.8 (±1%)	19.35 (±1%)	37 (±1%)
Bandwidth (MHz)	100 (±15%)	200 (±15%)	500 (±15%)	500 (±15%)
Integration time (ms)	200 (±15%)	200 (±15%)	200 (±15%)	200 (±15%)
Temperature sensitivity (K)	⩽0.5	⩽0.5	⩽0.5	⩽0.5
Linearity	⩾0.99	⩾0.99	⩾0.99	⩾0.99
3 dB beam width	E:15 ± 2° H:12 ± 2°	E:9 ± 2° H:9 ± 2°	E:9 ± 2° H:10 ± 2°	E:10 ± 2° H:10 ± 2°
Footprint (from 200 km orbital altitude) (km)	56	30	30	30

Table 2
Definition of MRM data at various level of preprocessing.

Levels	Data preprocessing description	Physical meaning
Raw data	Raw data is baseband data received from data transmission receiver in the two ground stations	Bit-stream data
Level 0A	Produced after the procedure of frame synchronization, descrambling and decompression. The coordinated universal time (UTC) was added	MRM source package data
Level 0B	Processed after sequencing, removing duplication and optimized stitching of Level 0A data, which were received from the two ground stations. The detached, format reorganized, stitched data, which were acquired in one calibrating and measurement period, were put into one MRM data block	MRM data block
Level 1	Several level 0B data block were incorporated into one track data file. The science data (sampled by observation antenna), temperature data (sampled at different part of the instrument), calibration data (sampled by cold space calibration antenna), auxiliary data were separated. MRM voltage data was produced after physical quantities conversion. After adding the description about the data and orbit parameter, level 1 data was produced	MRM voltage data
Level 2A	Firstly, antenna temperature were retrieved from level 1 MRM voltage data. Level 2A data was produced after the justification of data validity and rectification	MRM antenna temperature data
Level 2B	Level 2B data was produced after geometric positioning of MRM antenna temperature data	Positioned MRM antenna temperature data
Level 2C	Brightness temperature of the Moon, level 2C data, were retrieved from antenna temperature of level 2B data	Brightness temperature of the Moon

The Diviner Lunar Radiometer Experiment, onboard NASA's Lunar Reconnaissance Orbiter, observed the lowest temperature on the Moon down to 25 K, which occurred in the nighttime of north polar region, in its channel 9 thermal map (Paige, 2009). However, the spatial resolution of Diviner (about hundred meters) (Paige et al., 2010) is much finer than that of the CE-1 MRM (35–50 km), so the CE-1 TB data represent an average over a wider area. The least penetrative CE-1 TB data at 37 GHz is an average of a thin surface layer, but nonetheless much more penetrative than that obtained from the Diviner infrared sensor. Therefore the lowest possible CE-1 TB is likely to be higher than 25 K. Previous ground-based microwave observations suggest that TB values exceeding 500 K or lying below 30 K are very rare on the Moon (Hirth et al., 1976; Keihm and Gary, 1979; Battaglia, 2003; Morabito et al., 2008). Therefore we chose 30 K and 500 K as reasonable cut-off values to screen the CE-1 TB data, resulting in about 0.04% of the entries being eliminated using this criterion. To the best of our knowledge, we are not aware whether any of these eliminated "peculiar" data points repeat in the same location, under similar situations or exhibit any discernible regularity in pattern.

The processing steps are: (1). Select all level 2C data of the nominal flight period of the explorer. (2). Remove the explanatory header part in each file. (3). Combined all measurements in all tracks files into a single data file. (4). Use statistical software package to eliminate peculiar data having TB higher than 500 K or lower than 30 K.

3. Organizing the MRM TB data by lunar local time

According the circular polar tracks of CE-1's MRM, TB of the lunar surface was measured at different lunar local times, in terms of different solar incident and azimuth angles. As shown in Fig. 3 below, the diurnal variation of TB is large. Even within the lunar daytime, the values of TB in the morning and in the afternoon show large differences. Similar to the temperature variation on the Earth, TB is a strong function of local time. Therefore, it is important to clarify this dependence with a proper local time variable before any data processing and retrieving effort.

3.1. Hour angle as the lunar local time variable

In the MRM level 2C data, the local time for each observation record is characterized by two coordinates in the Horizon Coordinate System (HCS), the solar incidence and azimuth angle, which describe the position of the Sun with respect to the observer, as shown in Fig. 2a. However, since the local time should be latitude independent it is more formal to express the position of the Sun with respect to the celestial sphere using the Lunar Equatorial Coordinate System (LECS) instead.

Similar to the earthbound Equatorial Coordinate System (Montenbruck and Pfleger, 1994, p. 13), we can project the moon's equator onto the celestial sphere to define the *lunar celestial equator*. The LECS is basically the projection of the lunar latitude and longitude coordinate system onto the celestial sphere. Lines of latitude become lines of *declination* (*Dec*) and indicate how far north or south of the lunar celestial equator the object lies. Lines of longitude have their counter part in lines of *right ascension* (*RA*). In LECS, the right ascension and declination are the coordinates required to describe the position of a distant object in the sky. Unlike the HCS, these coordinates are independent of lunar observer's location and local time. Using the LECS, a natural measurement of the local time can be defined as the difference between the *solar right ascension* and the instantaneous *right ascension* of the local zenith (meridian), also known as the *hour angle* of the Sun.

Fig. 2b shows the relation between the HCS and the LECS at local noontime with the simplifying assumption that the small tilt (1.54°) between the lunar equatorial plane and the Ecliptic plane is ignored. Under this simple situation, the hour angle is zero and the solar incidence equals to the solar *declination*, which is same as the latitude of the observer. For more general situations, the

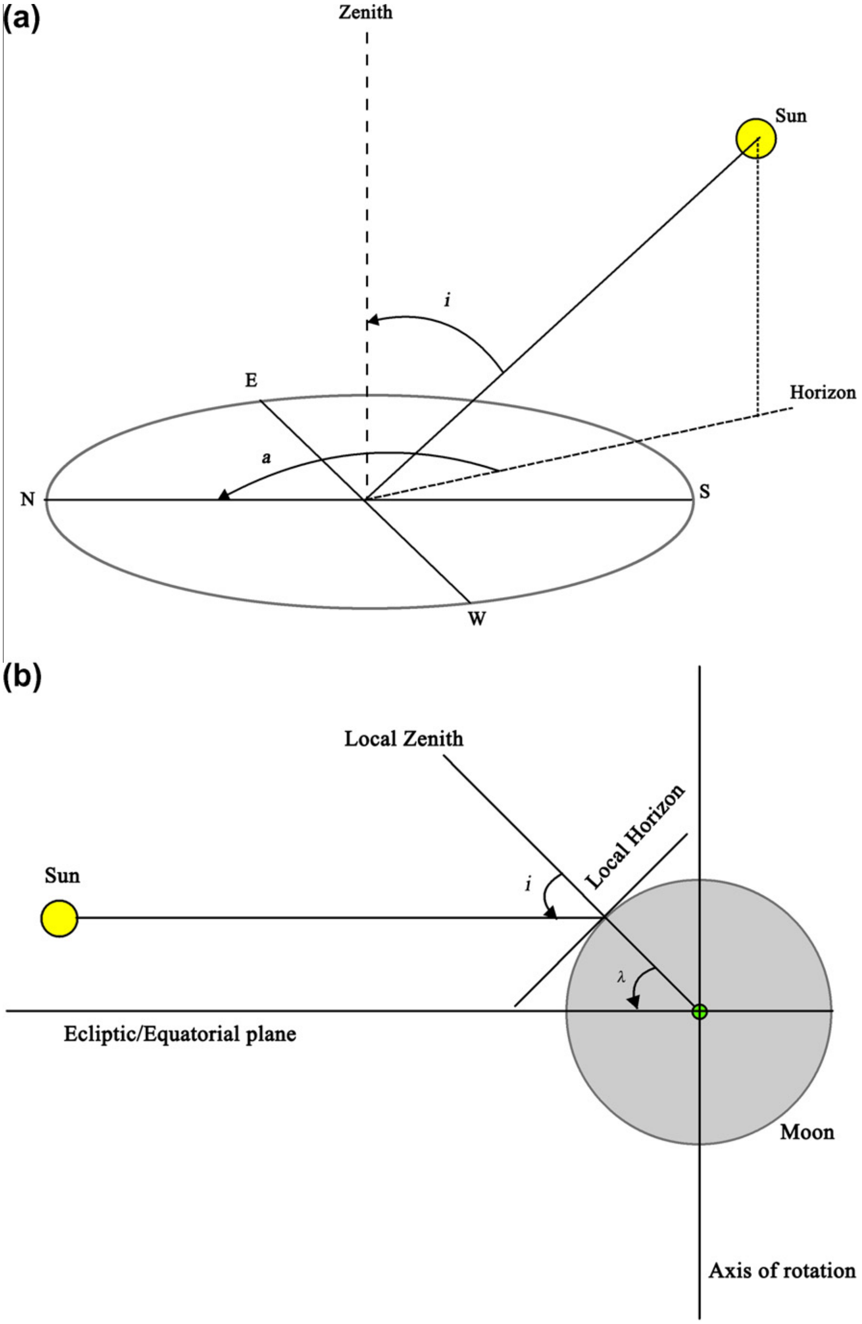

Fig. 2. The Lunar Horizon Coordinate System and Equatorial Coordinate System. (a) The Lunar Horizon Coordinate System: two angles, azimuth angle *a* and incident angle *i* are needed to specify the direction of the Sun. (b). The Lunar Equatorial Coordinate System at local noon time, ignoring the small tilt (1.54°) between the lunar equatorial plane and the Ecliptic plane. Direction of the Sun is specified by the latitude λ of the observer and the hour angle *h*, which is zero here. In this coordinate system, declination of the Sun is same as the latitude λ of the observer and the right ascension is equivalent to the hour angle *h*.

reader is referred to relevant literature (Montenbruck and Pfleger, 1994, Fig. 3.1).

The transformation between the HCS and the LECS leads to the following expression for the solar hour angle in terms of the solar incidence and azimuth angle (Montenbruck and Pfleger, 1994, Eq. (3.4)).

$$\tan h = \sin a \sin i/(\cos\lambda\cos i + \sin\lambda\cos a \sin i).$$

where is the i is the solar incident angle (zenith angle) $[0,\pi]$, a the solar azimuth angle (clockwise from north) $[0,2\pi]$, h the hour angle (negative before noon, positive after noon) $[-\pi,\pi]$ and λ is the lunar latitude $[-\pi/2,\pi/2]$.

With the above formulae, the range of daytime hour angle on the Moon are from −90° to +90° while the nighttime ranges are from −90° to −180° and from 90° to 180°. In particular, the hour angle for noontime is 0°, and ±180° corresponds to midnight.

As a result of introducing hour angle, the effect of the solar radiation on lunar TB becomes a function of three independent variables: longitude, latitude and hour angle.

3.2. Modeling of diurnal variation of TB

Due to the systematic decrease of TB values towards the two poles, diurnal variation of TB is modeled in a number of latitudinal

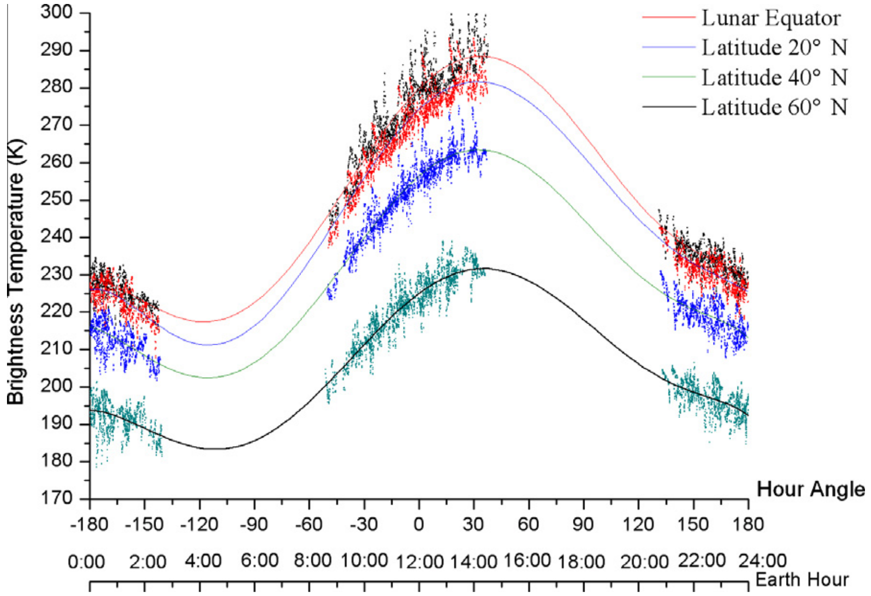

Fig. 3. CE-1's 37 GHz TB data at different latitude and its variation with lunar local time. The vertical and horizontal axes show TB and the hour angle respectively. Note that the diurnal variation of TB is about the same size as the variation from low to high latitudes.

Table 3
Parameters of the polynomial model at different latitudes (37 GHz data).

Data for fitting[a]	B	B_1	B_2	B_3	B_4	B_5	B_6	B_7	Adj. R-square	Fitting model applied[b]
0° ± 0.1°	279.87857	0.4928	−0.00605	−3.76E−05	2.41E−07	1.02E−09	−3.19E−12	−1.02E−14	0.9781	10°S–10°N
20°N ± 0.1°	274.35196	0.45137	−0.0063	−2.89E−05	2.68E−07	5.41E−10	−3.70E−12	−2.46E−15	0.97702	10°N–30°N, 10°S–30°S
40°N ± 0.1°	256.43028	0.41719	−0.00547	−3.19E−05	2.32E−07	8.90E−10	−3.18E−12	−9.64E−15	0.97377	30°N–50°N, 30°S–50°S
60°N ± 0.1°	225.04882	0.36032	−0.00416	−2.83E−05	1.81E−07	7.96E−10	−2.55E−12	−8.36E−15	0.95515	50°N–70°N, 50°S–70°S

[a] B data measured in the width of ±0.1° of latitude belts, were extracted to produce the fitting model.
[b] The fitting model was then applied in the width of ±10° of latitude belts.

bands each having a width of 20°. TB data within a narrow latitude extend (±0.1°) at the center of a band is used to build the diurnal model for the band so that the local variations along the same latitude due to topography and thermal or dielectric properties are smoothed out. The width of the latitude band (±0.1°) is determined from our experience with the MRM TB data. Due to the large size of the data set, if a wider band is chosen the number of data points included in the following numerical procedure would be too large and the calculation would be significantly slowed. If a narrower band is chosen, too few data would be involved and the result would not be as reliable.

After comparing a number of fitting methods that are commonly available in numerical software package, a degree-seven polynomial fitting scheme was chosen to provide a better fitting, to describe the general variation of TB versus local time in each latitudinal band:

$$TB_{h(model)} = B + B_1 \times h + B_2 \times h^2 + B_3 \times h^3 + B_4 \times h^4 + B_5 \times h^5 + B_6 \times h^6 + B_7 \times h^7$$

Here, h is the hour angle (in the range of $-180°$ to $180°$), $B, B_1, B_2, \ldots$ are constants, and $TB_{h(model)}$ is the model value at the hour angle h.

As an example, the fitting of models over a range of latitudes for the 37 GHz data are shown in Fig. 3. The fitted model parameters are given in Table 3. It is easy to conclude from Fig. 3 that in spite of the weak dependence of the fitting constants $(B, B_1, B_2, \ldots)$ on the latitude the diurnal variation of TB has about the same magnitude as the latitude varies from low to moderately high (about 60°) values. The coefficients of determination, R^2, which measure how well the fits agree with the data, are also shown in Table 3 for each case, so that the reader can judge the quality of our fits. These considerable diurnal variations suggest that: in the process of constructing a TB map, any failure to distinguish between the spatial and temporal effects will lead to the degradation of picture quality of microwave images.

3.3. Normalization of MRM TB data

In principle, the CE-1 TB data could cover the entire lunar surface many (about 8) times. However, they cover each local spot on the lunar surface at different local times, sometimes more frequently while other times less so. In other words, at any spot on the lunar surface, we may not be able to find the TB data that corresponds to its values measured exactly at noon or midnight. For the purpose of constructing a TB map at noon, we project with the formula below all daytime TB data to their noon time (hour angle 0°) value. Likewise, the nighttime TB data are projected to their midnight (hour angle 180°) value. For each point on the lunar surface, following projection formulae are as used to obtain its noon or midnight value:

$$TB_{noon(normalized)} = TB_{h(measured)} \times TB_{noon(model)} / TB_{h(model)}$$

$$TB_{midnight(normalized)} = TB_{h(measured)} \times TB_{midnight(model)} / TB_{h(model)}$$

where $TB_{h(measured)}$ is the TB data measured by MRM at hour angle h, $TB_{h(model)}$ the TB value given by the model (discussed in Section 3.2) at the local time h, $TB_{noon(model)}$ the fitted model TB value at noon, $TB_{midnight(model)}$ the fitted model TB value at midnight, $TB_{noon(normalized)}$

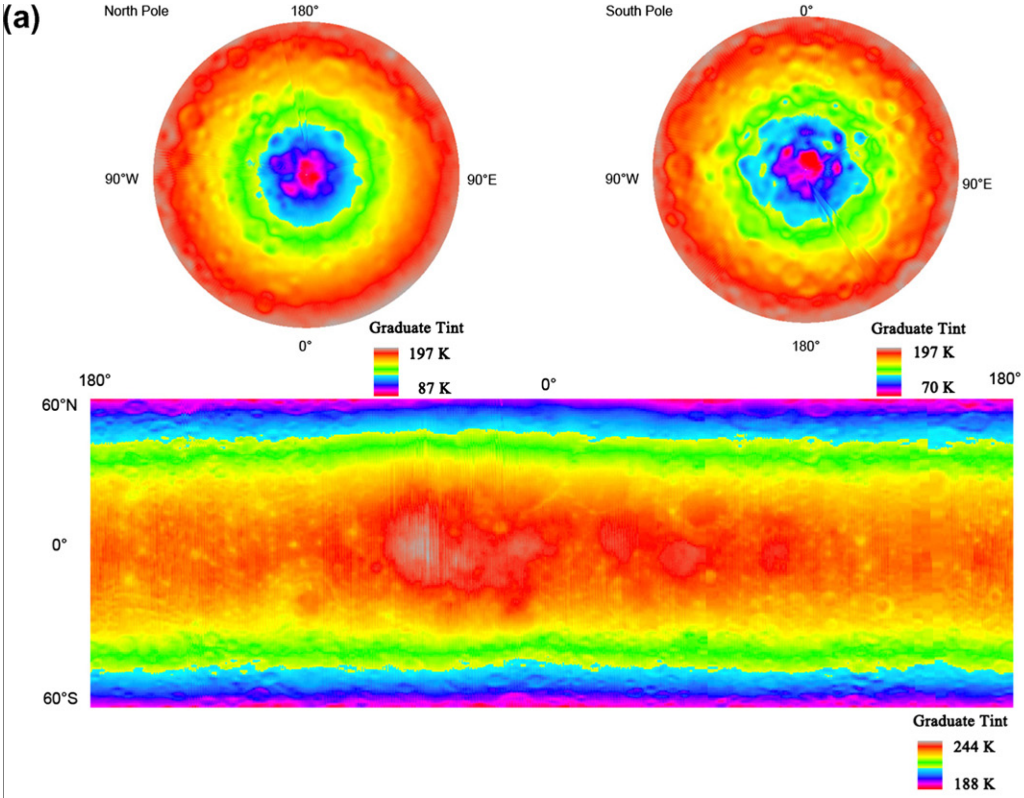

Daytime Brightness Temperature Map of The Moon from China's First Lunar Probe Chang'E-1 (3.0GHz)

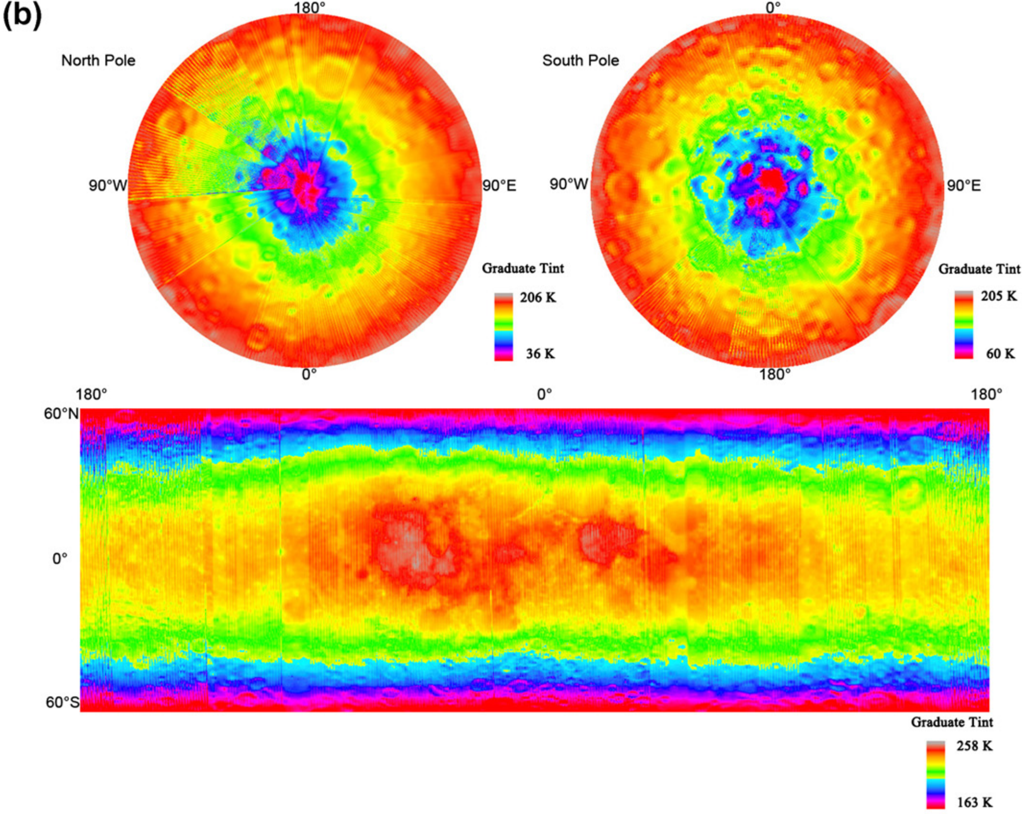

Daytime Brightness Temperature Map of the Moon from China's First Lunar Probe Chang'E-1 (7.8GHz)

Fig. 4. a-d. Daytime (noon) TB image of the Moon for the four channels. Except for the 7.8 GHz channel, data/image quality is high. TB for the same area increases with the measuring frequency, and so is the clarity of topographical features such as: craters, mountain ranges and the boundaries between mare and highland.

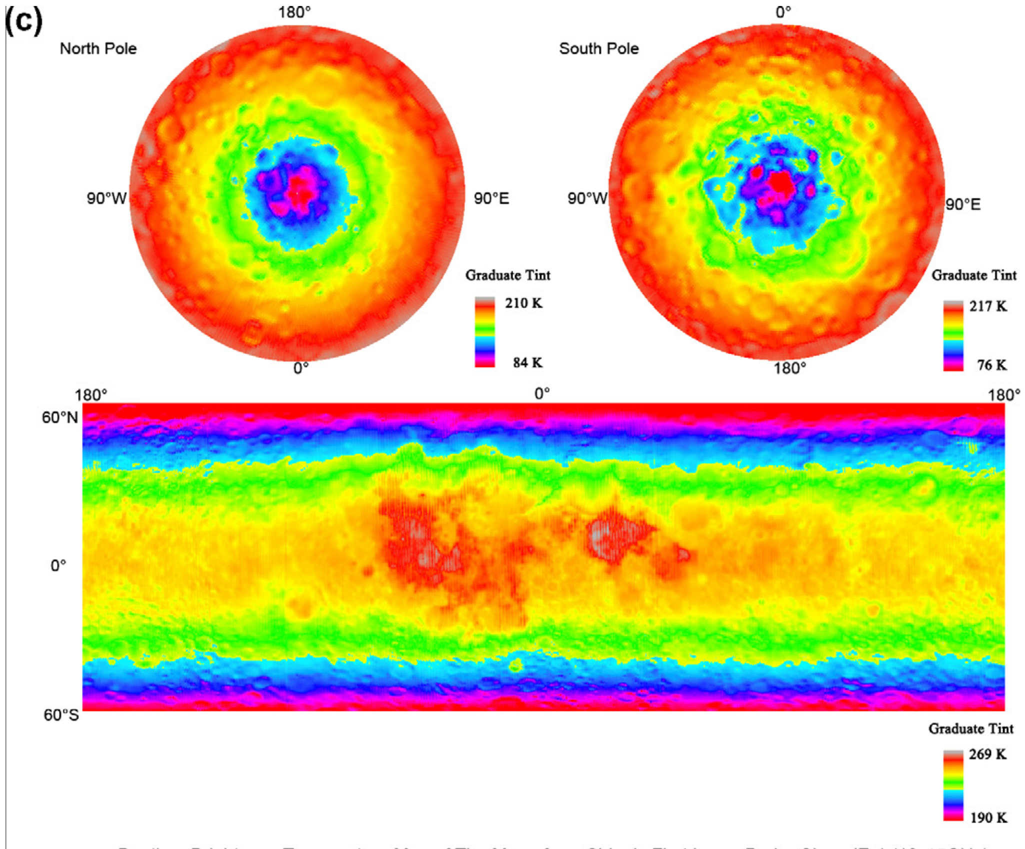

Daytime Brightness Temperature Map of The Moon from China's First Lunar Probe Chang'E-1 (19. 35GHz)

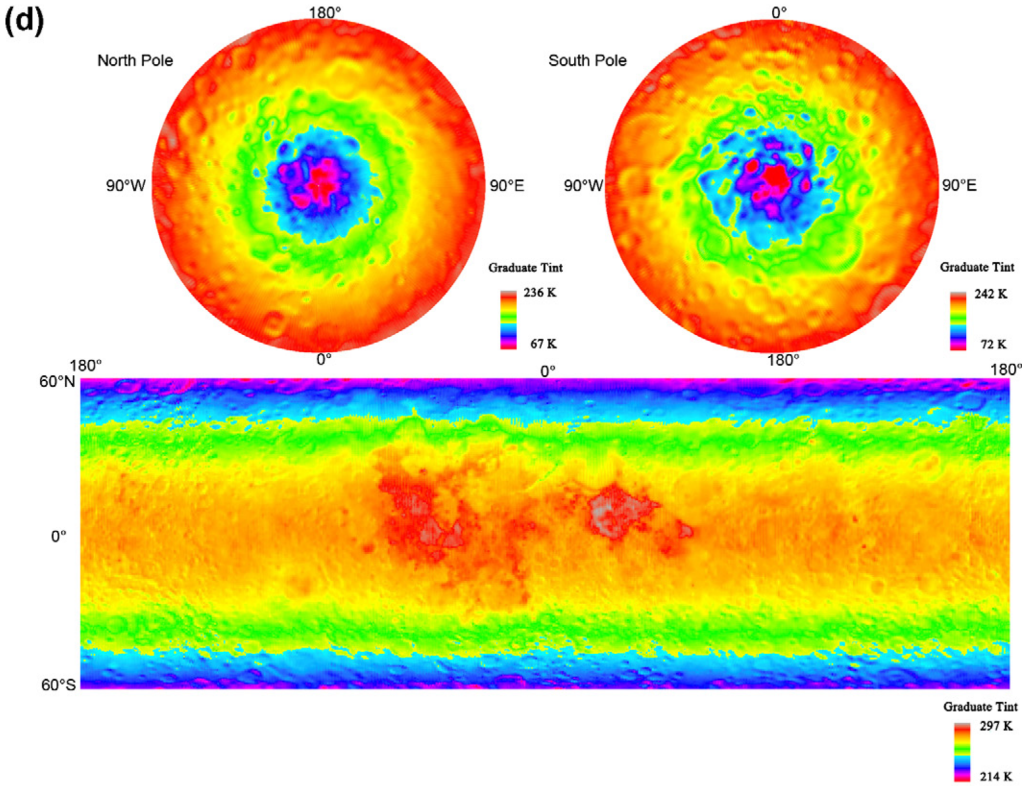

Daytime Brightness Temperature Map of The Moon from China's First Lunar Probe Chang'E-1 (37GHz)

Fig. 4 (*continued*)

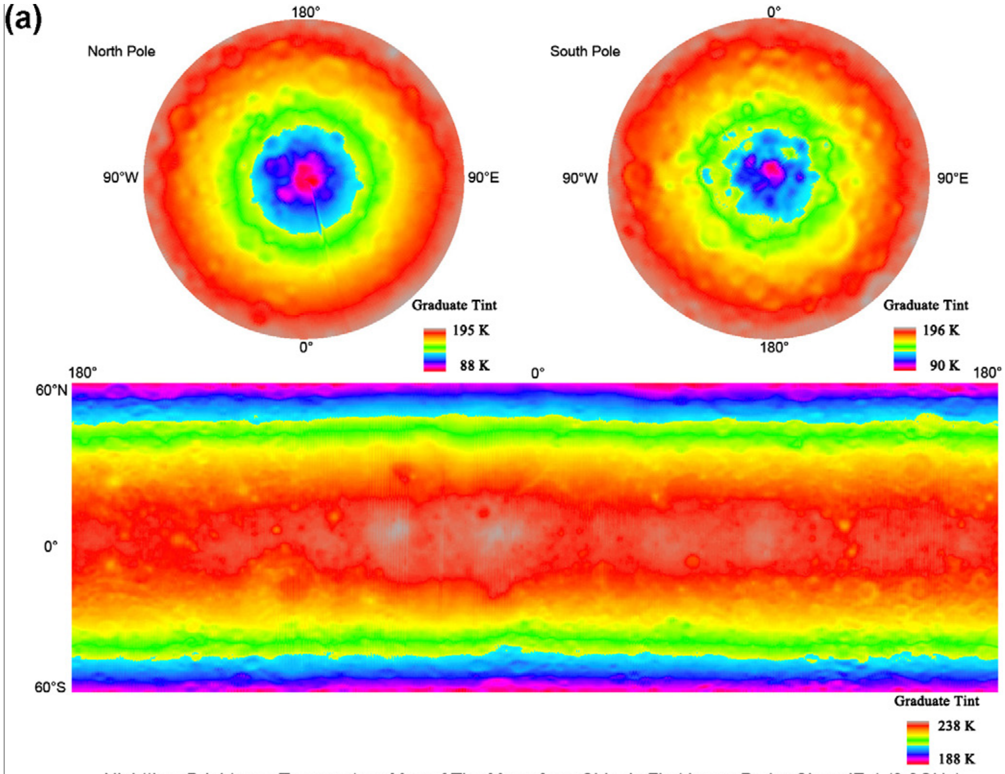

Nighttime Brightness Temperature Map of The Moon from China's First Lunar Probe Chang'E-1 (3.0GHz)

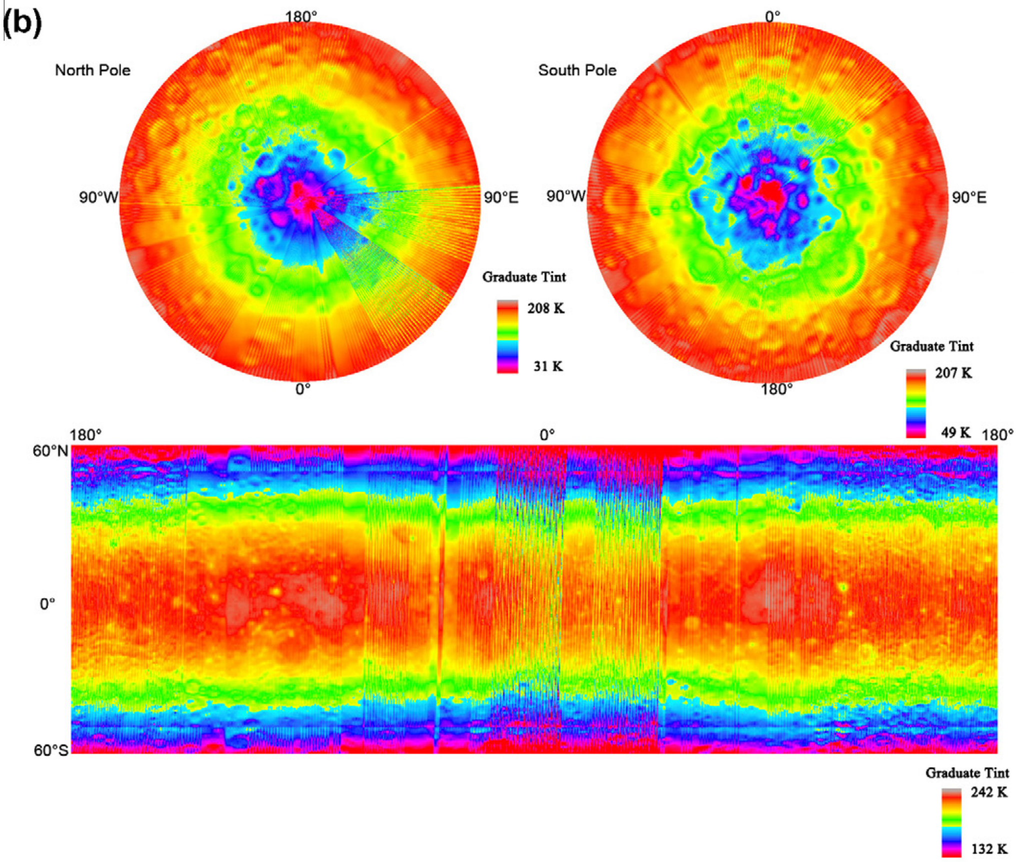

Nighttime Brightness Temperature Map of the Moon from China's First Lunar Probe Chang'E-1 (7.8GHz)

Fig. 5. a-d. Nighttime (mid-night) TB image of the Moon for the four channels. Except for the 7.8 GHz channel, data/image quality is pretty high. TB readings from different frequency channels for the same area differ by roughly 10 K. The most striking feature of the nighttime TB maps is the appearance of cool spots, whose number increases with the observing frequency as seen from a to d.

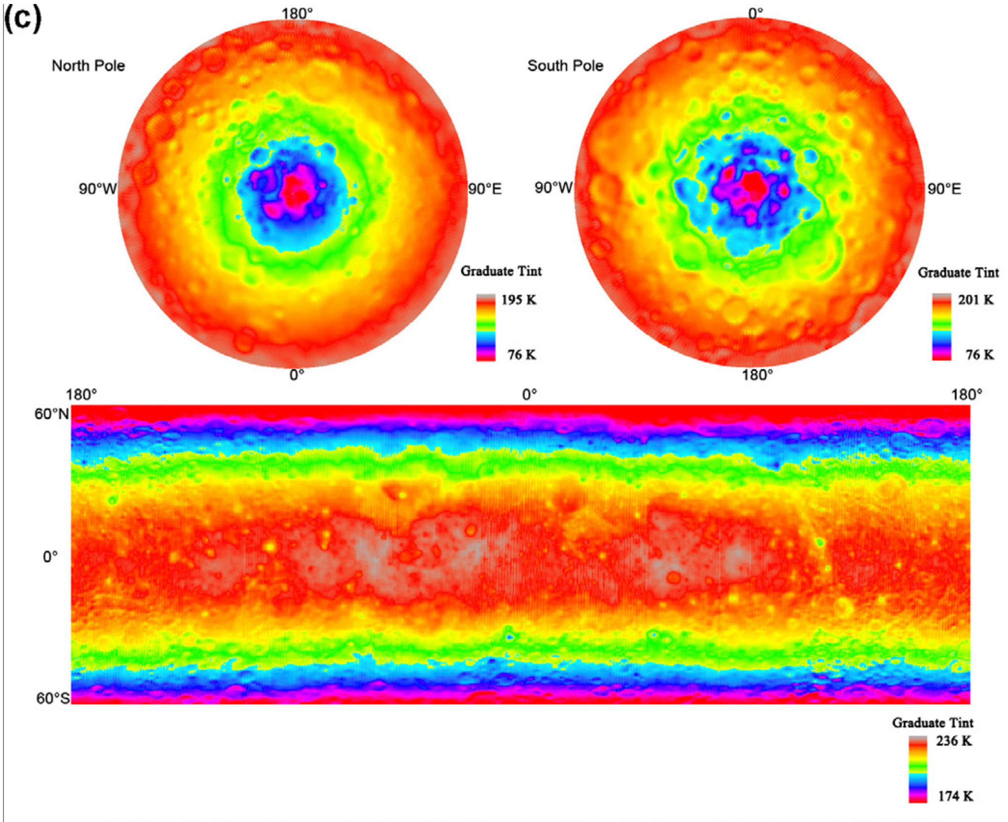

Nighttime Brightness Temperature Map of The Moon from China's First Lunar Probe Chang'E-1 (19.35GHz)

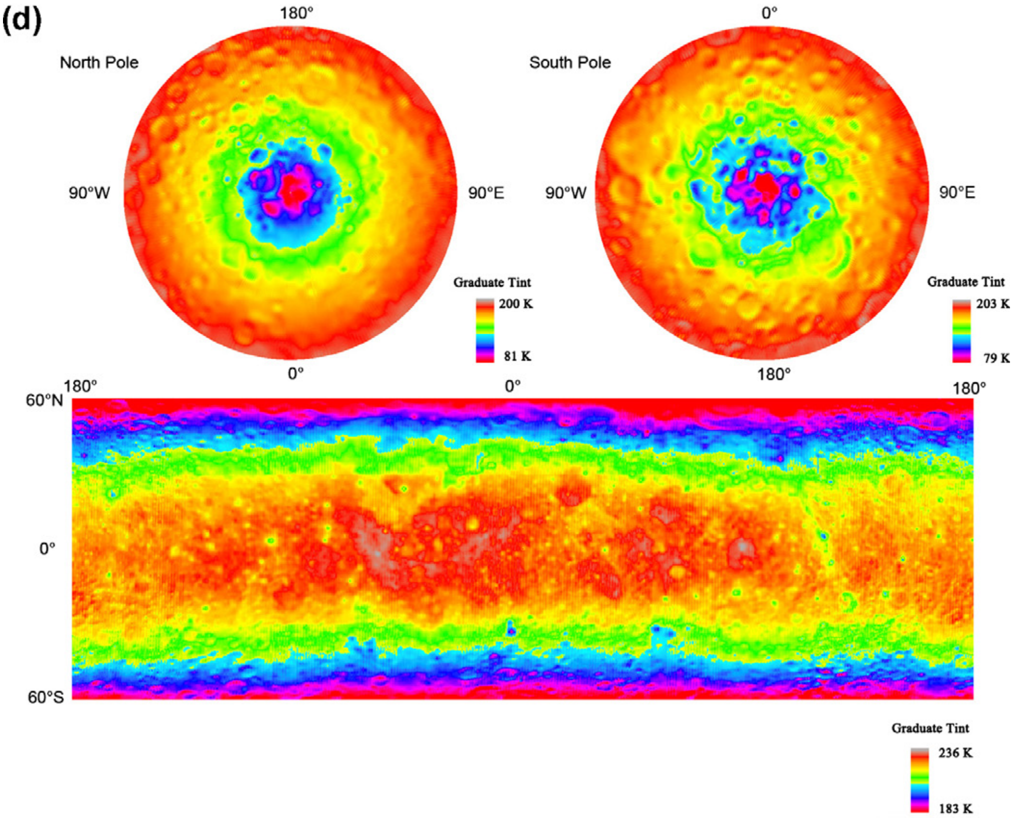

Nighttime Brightness Temperature Map of The Moon from China's First Lunar Probe Chang'E-1 (37GHz)

Fig. 5 (*continued*)

the normalized value of measured TB at noon, and $TB_{midnight(normalized)}$ is the normalized value of measured TB at midnight.

In essence, this scheme is a linear approximation to project the difference between the actual measured TB and the mean TB of the same latitude at the same local time to obtain a normalized noon (or midnight) value. In other words, we assume the dependence of TB on the hour angle within the same latitude band has the same functional form as the mean TB. With this numerical procedure, the measured TB at any location during any lunar local time can be projected from the CE-1 TB data within the accuracy of our model fit.

This procedure is an important improvement over previous efforts of some of us and other authors (Wang et al., 2010b; Zheng et al., 2010), which ignored the consideration of local time in the imaging process, in two regards. First, a single variable, the solar hour angle, is used to quantify the local time, instead of two variables: solar incident and azimuth. Second, the behavior of the TB data in this local time variable can be modelled by the fitted relationship.

4. Microwave maps of the complete Moon

4.1. Process of lunar microwave imaging

CE-1's MRM TB data provides not only complete global coverage of the lunar surface, but also the diurnal variation. In order to reveal the topographic information and other geological features hidden in the TB data, microwave maps are constructed using data rescaled to the same local time so that the resulting images are free from distortion due to local time effects. Here, in order to contrast the day–night moonscape scenes we will focus our attention to the noon and midnight images.

The final "normalized" microwave maps were constructed using GIS software with a simple cylindrical projection in low to medium latitudes. The high-latitude polar-regions are shown separately in azimuthal projection. The final resolution of the map produced is based on an interpolation scheme over a grid size of 0.5° × 0.5°. CE-1 went around the entire lunar globe once in 310 tracks. Hence, consecutive tracks have a mean separation of 1.16 degree in longitude. In order to fill the map pixels with a resolution of 0.5°, we need several rounds (each consists of roughly 310 tracks) of CE-1 track data, so that the gaps between the tracks can be gradually reduced to the desired resolution. However due to the uneven longitudinal distribution of the rounds of tracks, a small number of gaps remain even after a total of eight rounds of tracks (all available CE-1 data) have been used. It is possible to eliminate the lines by increasing the size of the pixels (for example, change the resolution to 1°), but then much information would be lost through the averaging process and the maps would not appear as sharp.

As a result of this procedure, the qualities of the maps were much better than those of previous studies (Wang et al., 2010b; Zheng et al., 2010). The procedure includes:

(1) The normalized TB values are fed into the GIS software, the vertical and horizontal coordinates are the latitude and longitude, respectively. The projection uses the coordinate system GCS_MOON_2000.
(2) Spatial interpolation is applied twice using inverse distance weighting.

In Figs. 4 and 5, TB images of the entire Moon in all four frequency channels are shown for both noon and midnight, respectively. Except for the second frequency channel (7.8 GHz), the level of sharpness of these images, especially the 37 GHz daytime image, is surprisingly high in comparison with previous work that mixed up TB data, which were measured at different local times. The sudden jumps in TB in the longitudinal direction in Figs. 4b and 5b are likely due to the comparatively lower quality of the 7.8 GHz MRM data. In the following we will focus our discussions on the data from the other three higher quality channels.

For comparison, as an example, in Fig. 6, we show a TB map obtained by following the 37 GHz TB data, in the same track by track sequence as observed by CE-1, without going through the trouble of renormalizing the data to the same local time (noon or midnight). Comparing either with Fig. 4d (noon) or Fig. 5d (midnight), it is obvious that Fig. 6 lacks the acuity in both of them, with a lot of the detail structures missing. With each track occurring roughly 127 min later than its previous track, the difference in local time between adjacent pixels is not significant enough to cause serious degradation to the picture quality. However, it is enough to introduce a level of blurriness in the overall image quality. Many fine structures clearly visible in Figs. 4d and 5d are lost in Fig. 6. More troubling is the appearance of a jump in TB values across the

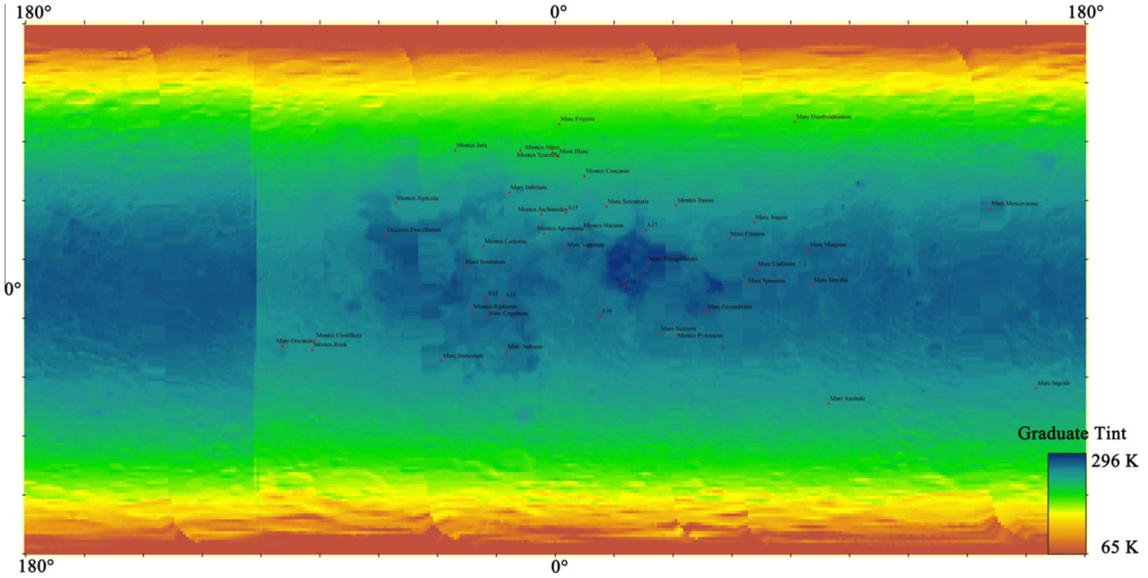

Fig. 6. TB map obtained by following the 37 GHz MRM 2C level data. We have not normalized the data to the same lunar local time (noon or midnight). 310 tracks of MRM data observed by CE-1, were combined track by track as in its sequence of polar orbits, which covered the complete Moon nicely.

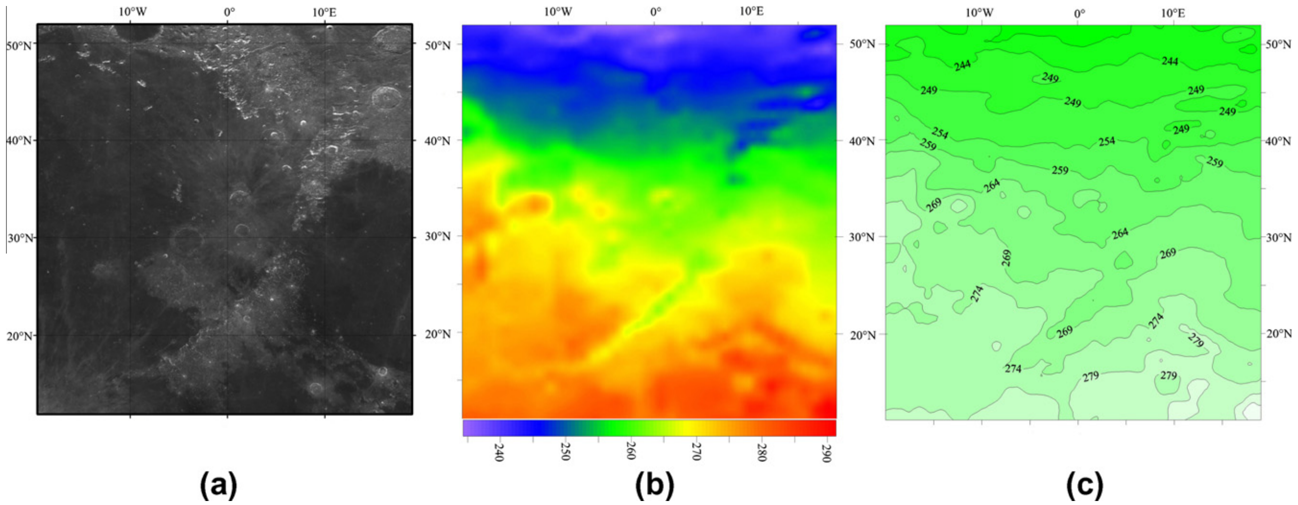

Fig. 7. (a–c) Noon-time 37 GHz TB image around Montes Apenninus. (a) CE-1 CCD image. (b) 37 GHz TB image layered with CE-1 DEM. (c) 37 GHz TB distribution. Comparing high elevation area of Montes Apenninus with Mare Imbrium of the same latitude, TB of higher elevation is lower than that of the low elevation flat mare.

(approximately) 100°W longitude, due to the accumulative effect of the small local time differences in adjacent tracks. After one complete revolution of orbits around the lunar globe, data from the starting track and the ending track (both of them near 100°W longitude) accumulated a considerable mismatch in local time, and thus a jump in TB is displayed.

Overall, these microwave images of the Moon have visual features that look familiar, but they contain very different physical information from the UV–VIS-IR images. A general impression one can discern from these images is that there are different temperature zones on the Moon that are quite similar to the tropical, temperate and frigid zones on the Earth. This is consistent with Clementine infrared observations (Lawson et al., 2000). Beyond this superficial impression, there are additional intriguing details that we will point out in the following discussions.

4.2. 3 GHz TB images: subsurface information

The mare-highland boundaries and craters' contour are fuzzier in the 3.0 GHz TB images (Fig. 4a) than the higher frequency images (Fig. 4b–d), because of the fact that the lower frequency emission can penetrate depths beyond several meters below the lunar surfaces (Zheng, 2005), in addition to the fact that spatial resolution of the MRM at 3 GHz is lower than those at higher frequencies. With such sensing ability, the 3.0 GHz TB data can be used to retrieve thermal properties of the lunar regolith and heat flow from the interior, as well as regolith thickness. The former result is very important for the study of thermal evolution of the Moon and the latter is useful for estimating the amount of helium-3 resources present in the lunar soil layers. Since the solar radiation effect is negligible during the lunar night, the 3 GHz nighttime TB data (Fig. 5a) is very valuable for retrieving physical parameters.

4.3. Daytime 37 GHz TB image: shadow and albedo effects

Almost all of the major craters and mountains could be identified easily in the daytime (noon) 37 GHz TB image of the Moon (Fig. 4d). This shows the strong influence of on the daytime TB image. From Fig. 4a–d, the topography contours in high frequency TB map are more clearly defined than those in low frequency TB map.

From Fig. 7, we can clearly differentiate the detailed temperature distribution around Montes Apenninus. Along the slope exposed to the Sun from northern Mare Serenitatis to Montes Caucasus, the temperature decreases with increasing latitude. We also found that the side exposed to the Sun, right side, is much warmer than the left side against the Sun, as seen around Montes Apenninus. This reaffirms that solar radiation is an important factor in determining the local TB, especially in high frequency TB maps.

Maria, which appear darker in visible images, show up brighter in the microwave images (Figs. 4 and 5). In general, visibly dark maria are hotter than surrounding highland regions during both daytime and nighttime. The boundaries between mare and highland terrain appear much sharper than those appearing in ground-based microwave maps. Except for topography influence, it suggests that the maria with low albedo have absorbed much more solar radiation than the bright highland. It leads to the general difference of TB values in the maria and highland at the same latitude band. Another factor is that the penetration depths of microwave radiation in highland are greater than those in maria. In general, the dielectric loss of basaltic regolith in maria are much higher than those of the anorthosite regolith in highland. As a result, the penetration depths of radiation in highland are much greater than those in maria. The measured TB in maria is primarily originated from the uppermost layer of the regolith (which are warmer/cooler during daytime/nighttime). The measured TB in highland, on the other hand, is contributed by a deeper and thermally more stable layer of the regolith.

In Fig. 8 (8a daytime, 8b nighttime), some major hot regions were outlined in the area of nearside maria. We have found two extremely hot regions during daytime on the nearside: South of Oceanus Procellarum and Mare Tranquillitatis. Among them, the crescent shaped region along the west side of Mare Tranquillitatis is the hottest spot on the Moon. During the nighttime, Oceanus Procellarum and Mare Vaporum remain the warmest region, while Mare Tranquillitatis cools down.

4.4. Nighttime 37 GHz TB image: discovery of cold spot

Due to the fact that the MRM is a passive system, microwave measurements can be performed in the absence of any solar illumination. The unobservable Moon in the visible band during the lunar night and in the permanently shadowed areas can be observed with the MRM.

The most striking feature of the 37 GHz nighttime microwave map (Fig. 5d) is that the entire lunar surface is dotted with many

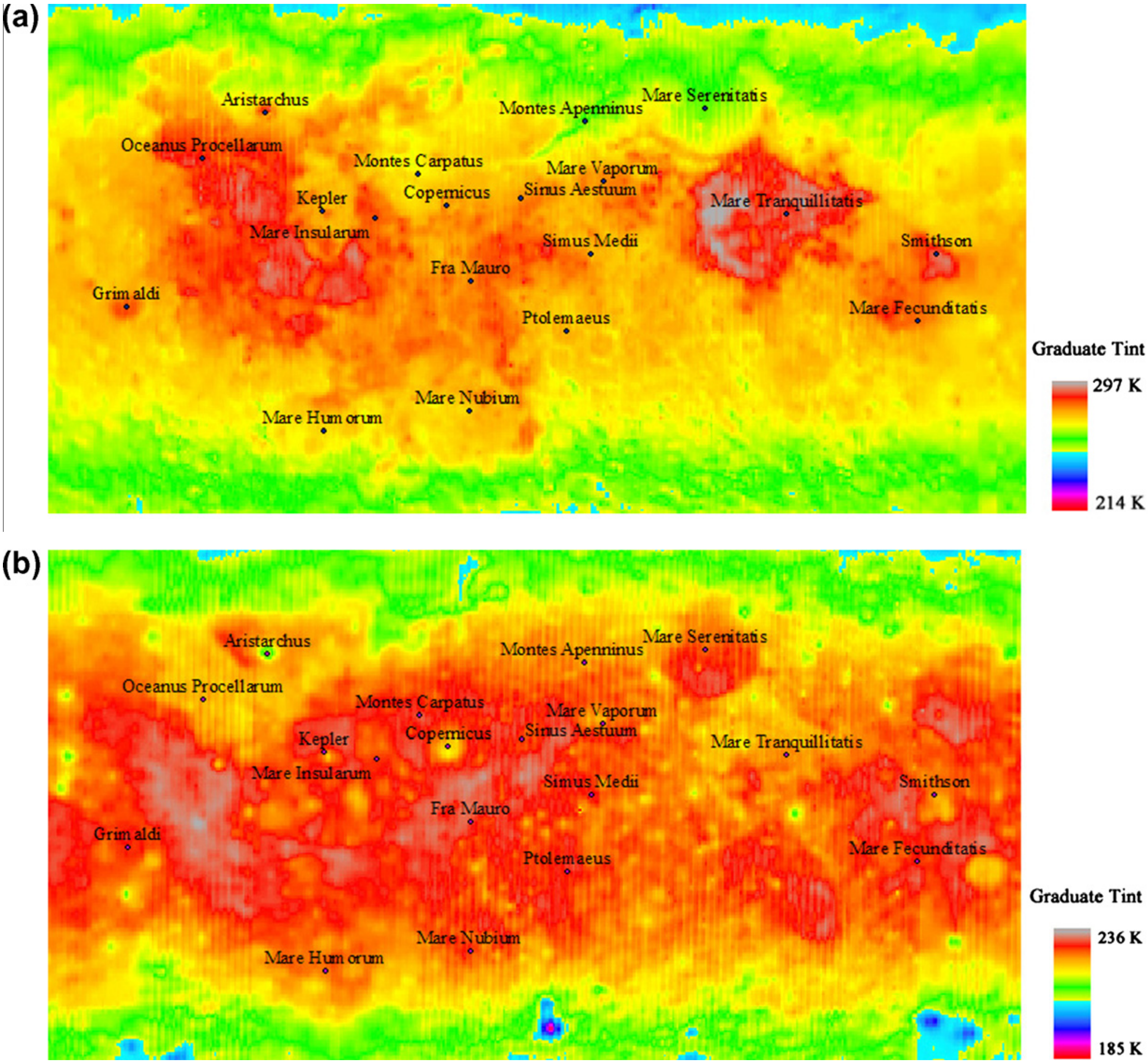

Fig. 8. Major hot regions on the Moon (37 GHz TB image). (a) Noon-time and (b) midnight. Two hot regions of the Moon in the daytime are found: South of Oceanus Procellarum and Mare Tranquillitatis. The diurnal variations of TB in Mare Serenitatis and Mare Transquillitatis are entirely different. Mare Serenitatis is relatively cold in the daytime and but warmer in the nighttime whereas Mare Transquillitatis is the other way around. As described in Section 4.1, interpolation scheme was employed by the GIS software in the process of lunar microwave imaging. The small size of the pixels leads to some blank vertical lines in the map where no track passes through. However, they have no influence on the information provided by the TB distributions.

relatively cool spots compared with surrounding areas. These cool spots have been identified same as the hot areas during lunar eclipses (Price and Mizuno, 2003; Shorthill and Saari, 1965). We also have found that these cool areas in the nighttime moonscape were located in relatively young craters, which were formed in younger Copernican periods, with bright radial rays and round deep morphology, such as Crater Aristarchus, Giordano Bruno, King, Lents (Fig. 9a–d). Due to the larger surface areas of these bowl-shaped craters, radiative heat exchange can be faster than that of a smooth/flat topography. That may possibly explain why the young craters are hotter in the daytime and colder in the nighttime than the surrounding areas, as shown in the 37 GHz TB map. However, during the short time period (several hours) of lunar eclipse, the craters do not have enough time to cool down. So the craters are still hotter than the surrounding areas.

4.5. Diurnal TB variation in the polar region

The TB data observed at the high frequency channel was mainly contributed by the emission from a thin layer (of a few centimeters) just below the lunar surface and directly related to the surface physical temperature (Zheng, 2005). With the advantages of having access to potential water ice, and long hours of solar illumination, the polar region is the favorite site for lunar base construction (Sharpe and Schrunk, 2003; Siegfried, 1999). An area on the rim of Crater Shackleton in the south pole, that is almost permanently sunlit and also adjacent to a permanently dark region, has already received high marks (Campbell et al., 2006; Nozette et al., 2001). Therefore, lunar day and night temperature, and its diurnal variation in the polar region, bears special significance to future human lunar exploration activities.

In the 37 GHz TB image of the south pole region (Fig. 10a and b), the coldest areas are located around the pole. The colder areas in the daytime, which correspond to the permanent shadowed regions remain colder in the nighttime.

From the perspective of diurnal TB variation, we have found three relatively temperate areas (Fig. 10a and b), which is warmer than their surrounding areas both in the daytime and nighttime. They are located at: north-west of Crater Wapowski, west of Crater Kocher, and west of Crater de Gerlache, respectively. We suggest

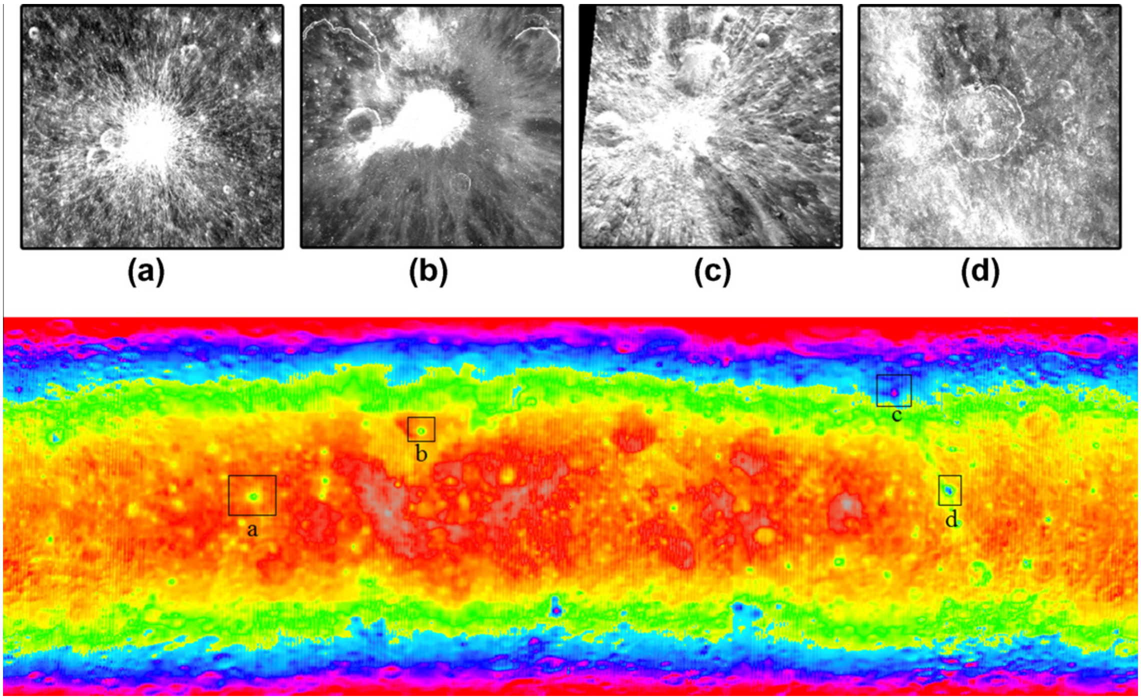

Fig. 9. (a–d) Cool areas in the midnight TB image. (a) Near Crater Lents. (b) Crater Aristarchus. (c) Crater Giordano Bruno. (d) Crater King. The images were photographed by CE-1 CCD stereo camera. All these craters have bright rays and much younger than the surrounding surface. Locations of these craters are boxed in the lower panel, which is the same image shown in Fig. 5d.

that more follow-up work should be performed on these three sites to evaluate their potentials as future human lunar base (Nozette et al., 1996).

5. Discussion

In this section, additional applications of the TB data processing technique presented in Section 3 are discussed. First, from the numerical relationship (Section 3.2) between TB and lunar local time, the time of occurrence of the highest and lowest temperature during a lunar day along any latitude can be determined. Second, as a by-product of our analysis, a normalized brightness temperature deviation can be defined to isolate the deviation of measured TB value away from the expected mean behavior determined by local time and latitude. This normalized TB deviation is attributable to other factors, such as local abundance of highly lossy materials in the regolith, shadow and albedo effect in different topographic unit. Following this reasoning, a correlation study between the normalized TB deviation and the TiO_2 distribution retrieved from Clementine UV–VIS-IR data (Lucey et al., 2000) is performed. The normalized daytime TB deviation is found to show substantial correlation with TiO_2 when its abundance is high enough.

5.1. TB extremes encountered during a lunar day

According to our regression model, the hour angles of the highest and lowest (latitudinal mean) TB are shifted away from noon and midnight (Fig. 3). The highest TB at the center of the nearside lunar disk occurs 2.76 days (about 9% of the lunar phase cycle) after the full Moon, while the lowest value occurs 5.12 days (about 17% of the lunar phase cycle) after the new Moon.

Table 4 shows the local times of the highest and lowest TB at different latitude bands. For the 37 GHz channel, the occurrence of the highest TB shifts to later local time as we move from the equator to the pole. The local time of the highest TB is delayed from an hour angle of 30° from noon at the equator to 54° at 80°N, but irregularities do exist in between due possibly to regional differences of the regolith. On the other hand, the time of occurrence of the lowest TB follow different rules. During lunar nights, the regions at high latitudes cool down faster than regions at low latitudes. The time when TB attains its lowest value is moved ahead from hour angles −117.59° at equator to −106.76° at 80°N. The dependence in TB with lunar latitude at 37 GHz is similar to the latitudinal influence of the surface temperature on the Earth.

For the 3 GHz channels, no similar latitudinal influence of TB value was observed. It suggests that the TB value at 3 GHz is influenced by many factors, not only surface temperature, but also subsurface temperature, thickness of lunar regolith layers, heat flow from the interior of the Moon, and heat flow from the interior of the Moon, among other factors.

5.2. Correlation between TB and titanium content of the lunar surface

In general, hot regions in the daytime TB image are found to coincide well with areas of high titanium abundance, e.g. Mare Tranquillitatis. We've tried to correlate the TiO_2 distribution retrieved from Clementine UV–VIS-IR data (Lucey et al., 2000) with the scaled brightness temperature deviation map ($TB - TB_{(mean)}$, as given in our previous paper (Chan et al., 2010)) for the latitude range from −60° to +60°. However, if the correlation is computed for the whole Moon, the correlation is very low. This is due to the inclusion of large 'irrelevant' areas which contain no TiO_2 nor significant temperature deviation, yet these areas dominate the statistics. We can minimize the impact of such sampling contamination by considering only regions where the estimated TiO_2 content exceeds a certain threshold value. Regions with cutoff values at 0, 3, 6, and 9 wt.% (percentage content by weight) of TiO_2 on the Moon are shown in the Fig. 11.

The 'conditional correlation' can be defined as $C_f = \langle \tau \mathrm{Ti} \rangle_f / (\langle \tau^2 \rangle_f \langle \mathrm{Ti}^2 \rangle_f)^{1/2}$, where τ is the normalized brightness temperature

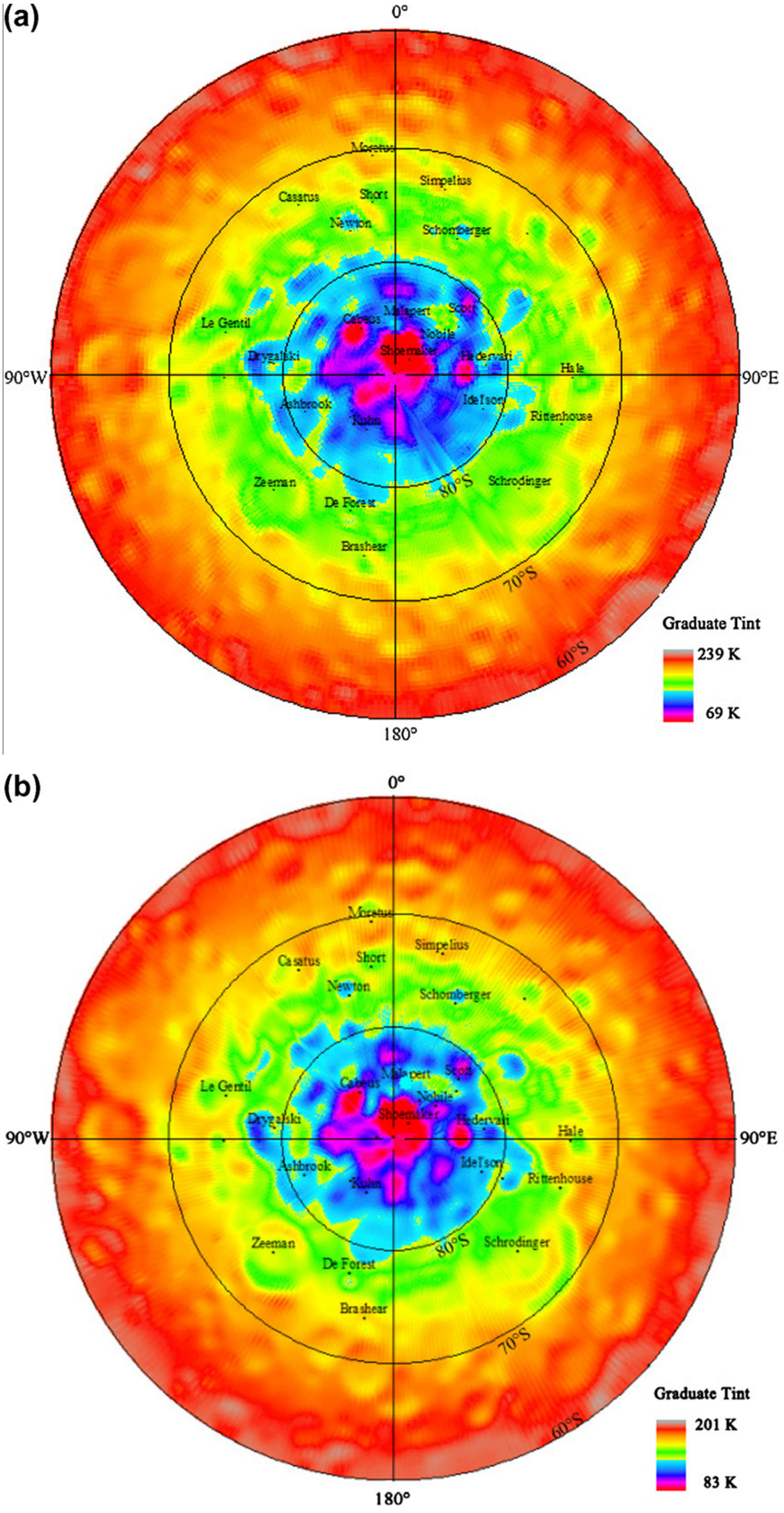

Fig. 10. (a and b) Daytime and nighttime 37 GHz TB maps for the south pole of the Moon. (a) Noon-time and (b) midnight. NW of Crater Wapowski, West of Crater Kocher, and West of Crater de Gerlache are the three relatively temperate areas.

deviation, i.e. $[TB_{t(measured)} - TB_{t(model)}](TB_{noon(model)}/TB_{t(model)})$, Ti is the percentage of titanium content, the angle brackets $\langle\rangle_f$ denotes summation over areas with Ti above a percentage f. Table 5 lists the conditional correlation for f values 0–9%. Note that the noise level of the TiO_2 map is on the order of 1%. A visual illustration of the behavior of the coefficients is given in Fig. 12 which plots

Table 4
The highest and lowest TB at different latitude bands.

Channel (GHz)	Latitude	TB_{max}	Hour angle	TB_{min}	Hour angle
37	0° ± 0.1°	288.54	33.64	217.46	−117.59
37	20°N ± 0.1°	281.74	31.77	211.26	−115.15
37	40°N ± 0.1°	263.38	32.27	202.41	−115.53
37	60°N ± 0.1°	231.61	35.09	183.33	−111.46
37	80°N ± 0.1°	169.98	54.05	136.34	−106.76
3	0° ± 0.1°	238.31	40.36	229.78	−99.71
3	20°N ± 0.1°	234.26	43.73	225.86	−100.21
3	40°N ± 0.1°	219.82	34.38	212.83	−103.12
3	60°N ± 0.1°	194.46	24.96	188.79	−97.72
3	80°N ± 0.1°	142.03	63.74	140.97	−113.7

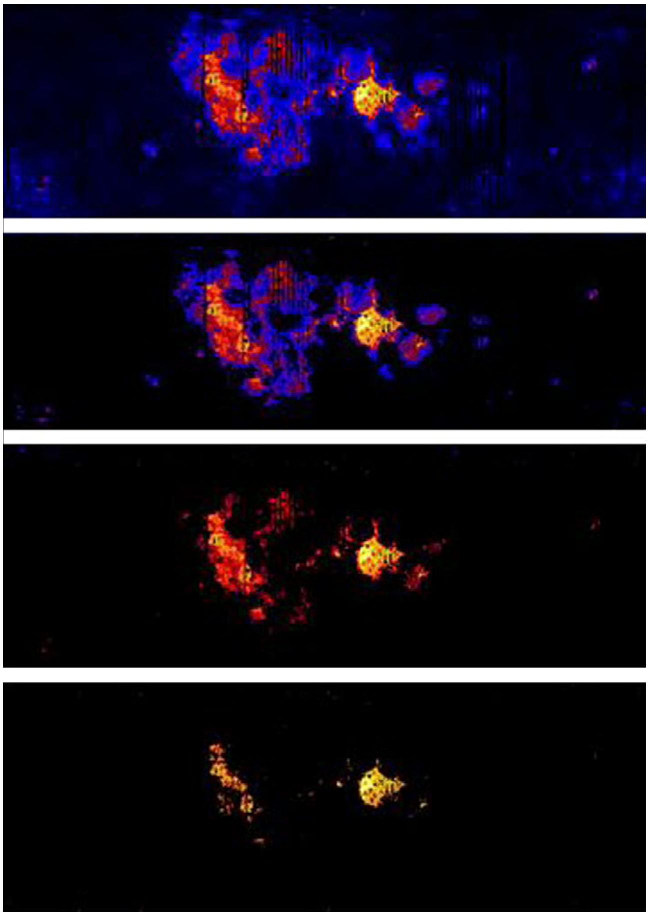

Fig. 11. The regions with TiO_2 content higher than 0, 3, 6, and 9 wt.% on the Moon. From top to bottom panel, the regions with TiO_2 content higher than 0, 3, 6, and 9 wt.% are shown.

the highest- and lowest-frequency correlation coefficients versus the cutoff percentage (0–9%) for day (left panel) and night (right panel). In daytime, C_f increases with higher cutoff thresholds, and it can reach rather high values. A surprise is that only the daytime temperature deviations show substantial correlations with TiO_2. The anticipated negative correlation with nighttime temperature deviation is not realized in general, unless when the cutoff level is set to be very high. This indicates that the nighttime cold spots found in our earlier paper may not be related to the abundance of TiO_2. The correlation coefficients between daytime temperature deviations and TiO_2 behave similarly in all four channels.

An interpretation of this result is that the high lossy ilmenite in mare basalt, with dark color and low albedo, has stronger absorption power for the solar radiation than the low lossy plagioclase in highland anorthosite, with bright color and high albedo. Due to this coincidence of the high daytime TB region with the area rich in ilmenite and helium-3, the western edge of Mare Tranquillitatis may be a good candidate for further exploration.

6. Conclusion

The most important contribution of this work is the introduction of the solar hour angle as an independent variable to characterize the effect of local time on the TB data. A regression model to post-process the CE-1 MRM TB data is then described in detail to produce the first microwave map of the complete Moon without the distortion due to mixing spatial and temporal effects. With the effect of local time on TB properly addressed by this methodology, a series of high quality TB maps over the entire lunar surface can be produced, showing details not seen in previous publications. With regard to the maps we have produced, the following statements can be made:

(1) For the first time, humans are capable of globally mapping the Moon during any lunar local time, using passive, multi-frequency, microwave remote sensing technology from an orbiting spacecraft, with significantly improved spatial resolution and temperature sensitivity.
(2) Due to the penetrative power of microwave emissions, hidden geological features below the lunar surface not observable in visible spectrum may be revealed by microwave images. The microwave images we present here will undoubtedly provide us with a new window to study the lunar surface, as well as a useful tool to probe the physical and geological properties of the sub-surface regolith layer.
(3) From this high resolution microwave map, we can immediately identify a crescent-shaped region in western Mare Tranquillitatis as the hottest area on the daytime Moon.
(4) Since microwave data can be acquired by MRM independent of solar illumination, this advantage of microwave imaging technology allows us to "see" the nighttime moonscape

Table 5
The 'conditional correlation' between TiO_2 and TB.

f value	3 GHz day	7.8 GHz day	19.4 GHz day	37 GHz day	3 GHz night	7.8 GHz night	19.4 GHz night	37 GHz night
0	0.3	0.11	0.37	0.28	0.02	−0.24	−0.1	0.01
1	0.73	0.56	0.79	0.63	0.25	−0.33	−0.03	0.21
2	0.82	0.76	0.88	0.78	0.34	−0.41	−0.04	0.26
3	0.84	0.82	0.91	0.83	0.35	−0.46	−0.11	0.24
4	0.86	0.85	0.92	0.87	0.34	−0.5	−0.21	0.17
5	0.86	0.87	0.94	0.9	0.31	−0.54	−0.32	0.01
6	0.87	0.89	0.95	0.93	0.27	−0.59	−0.44	−0.01
7	0.87	0.89	0.96	0.95	0.18	−0.63	−0.56	−0.22
8	0.87	0.91	0.96	0.96	0.05	−0.68	−0.69	−0.43
9	0.88	0.92	0.97	0.97	−0.16	−0.74	−0.8	−0.64

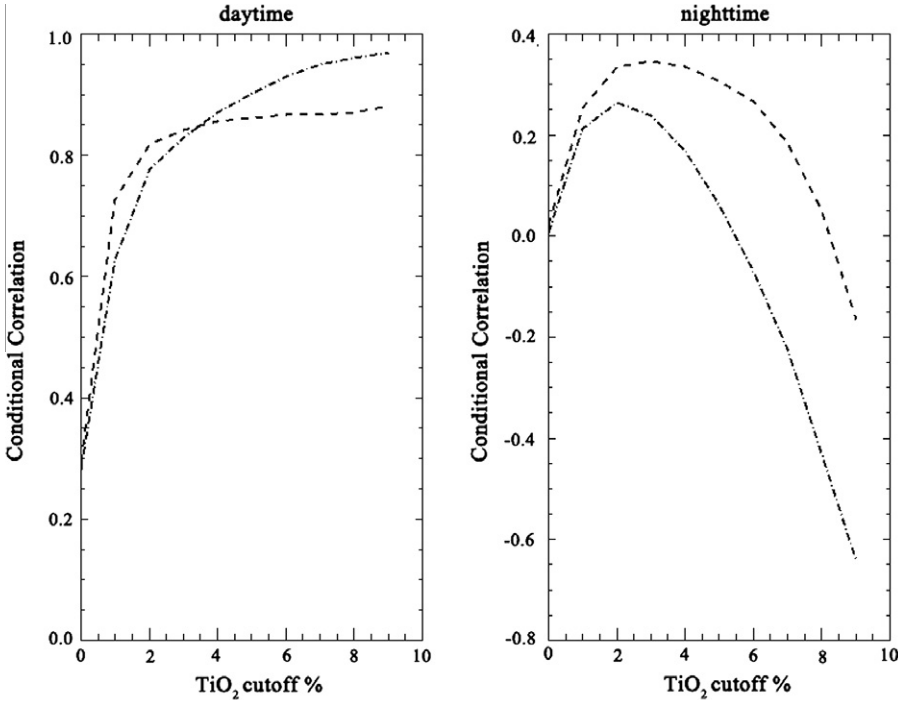

Fig. 12. Conditional correlation coefficients between TB and titanium versus cut-off TiO_2 content (0–9 wt.%). The left and right panels are for daytime and nighttime TB data, respectively. The dashed and dashed-dotted curves are for 3 GHz and 37 GHz, respectively.

and the permanently shadowed areas in the polar region without the aid of solar illumination. The most striking feature of the nighttime microwave image is that the entire lunar surface is dotted with many cool spots. These hitherto unreported "lunar cool spots" may be tentatively explained by the young local crater morphology where these spots are located, contingent on more evidence.

(5) In the lunar south-pole region, we have found three "polar comfort zones", which are considerably warmer than their surrounding areas both in the day and night. We suggest more follow-up work to evaluate the potential of these three sites as candidates for future lunar bases.

(6) Brightness temperature of the Moon in microwave bands can provide us with information on detail thermal characteristics of the lunar surface. Global temperature distribution and its diurnal variation are important factors to consider for the thermal shield design of lunar modules and rovers in the future unmanned and manned landing missions.

Acknowledgments

We gratefully thank the two reviewers for their careful reading and valuable suggestions. We thank Academician J.S. Jiang, Prof. X.H, Zhang and the MRM instrument group in National Space Science Center, Chinese Academy of Science (CAS), prof. C.L. Li, J.Z. Liu, H.B. Zhang and the GRAS group in National Astronomical Observatories, CAS. All engineers and scientists who contribute to the successful CE-1 mission would be sincerely thanked. This work was supported by National Science Foundation of China (40904051), the 863 Program (2009AA122201 and 2009AA122204), the Research Competitive Program of HKUST (RPC10SC09) and the Hong Kong Scholar Program.

References

Battaglia, M., 2003. Moon Disc Temperature as a Function of Phase at 1700 MHz. ETH Zürich, Switzerland.

Campbell, D.B. et al., 2006. No evidence for thick deposits of ice at the lunar south pole. Nature 443, 835–837. doi:10.1038/nature05167.

Chan, K.L., Tsang, K.T., Kong, B., Zheng, Y.C., 2010. Lunar regolith thermal behavior revealed by Chang'E-1 microwave brightness temperature data. Earth Planet. Sci. Lett. 295 (1–2), 287–291.

Fa, W.Z., Jin, Y.Q., 2007a. Simulation of brightness temperature from lunar surface and inversion of regolith-layer thickness. J. Geophys. Res. 112, E05003. doi:10.1029/2006JE002751.

Fa, W.Z., Jin, Y.Q., 2007b. Quantitative estimation of helium-3 spatial distribution in the lunar regolith layer. Icarus 190, 15–23.

Fa, W.Z., Jin, Y.Q., 2010. Analysis of microwave brightness temperature of lunar surface and inversion of regolith layer thickness: Primary results of Chang-E 1 multi-channel radiometer observation. Sci. China Ser. E 53, 168–181.

Feng, J.Q., Zou, Y.L., Bian, W., Zheng, Y.C., Li, C.L., 2010. Review on physical models of lunar brightness temperature. Chin. J. Geochem. 29, 204–211.

Gary, B.L., Keihm, S.J., 1978. Interpretation of ground-based microwave measurements of the Moon using a detailed regolith properties model. Lunar Planet. Sci. 9, 2885–2900.

Hagfors, T., 1971. Microwave studies of thermal emission from the Moon. Advances in Astronomy and Astrophysics, vol. 8. Academic Press, New York, pp. 1–28.

Hirth, W., Butz, M., Fuerst, E., Greve, A., 1976. The brightness distribution over the Moon's disk at 6 cm wavelength. The Moon 15, 317–323.

Keihm, S.J., 1982. Effects of subsurface volume scattering on the lunar microwave brightness temperature spectrum. Icarus 52, 570–584.

Keihm, S.J., 1984. Interpretation of the lunar microwave brightness temperature spectrum – Feasibility of orbital heat flow mapping. Icarus 60, 568–589.

Keihm, S.J., Cutts, J.A., 1981. Vertical-structure effects on planetary microwave brightness temperature measurements – Applications to the lunar regolith. Icarus 48, 201–229.

Keihm, S.J., Gary, B.L., 1979. Comparison of theoretical and observed 3.55 cm wavelength brightness temperature maps of the full Moon. Lunar Planet. Sci. 10, 2311–2319.

Lawson, S.L., Jakosky, B.M., Park, H.S., Mellon, M.T., 2000. Brightness temperatures of the lunar surface: calibration and global analysis of the Clementine long-wave infrared camera data. J. Geophys. Res. 105 (E2), 4273–4290.

Li, C.L. et al., 2010. The global image of the Moon obtained by the Chang'E-1: Data processing and lunar cartography. Sci. China Ser. D 53, 1091–1102.

Lucey, P.G., Blewett, D.T., Jolliff, B.L., 2000. Lunar iron and titanium abundance algorithms based on final processing of Clementine ultraviolet–visible images. J. Geophys. Res. 105, 20297–20305.

Montenbruck, O., Pfleger, T., 1994. Astronomy on the Personal Computer. Springer-Verlag, Berlin.

Montopoli, M., Di Carlofelice, A., Tognolatti, P., Marzano, F.S., 2011. Remote sensing of the Moon's subsurface with multifrequency microwave radiometers: A numerical study. Radio Sci. 46, RS1012. doi:10.1029/2009RS004311.

Morabito, D.D., Imbriale, W., Keihm, S.J., 2008. Observing the Moon at microwave frequencies using a large-diameter deep space network antenna. IEEE. Trans. Ant. Prop. 56 (3), 650–661. doi:10.1109/TAP.2007.915471.

Muhleman, D.O., 1972. Microwave emission from the Moon. In: Lucas, J.W. (Ed.), Thermal Characteristics of the Moon, vol. 28. MIT Press, Cambridge, pp. 51–81.

Nozette, S. et al., 1996. The Clementine bistatic radar experiment. Science 274 (5292), 1495–1498. doi:10.1126/science.274.5292.1495.

Nozette, S., Spudis, P.D., Robinson, M., Bussey, D.B.J., Lichtenberg, C., Bonner, R., 2001. Integration of lunar polar remote-sensing data sets: Evidence for ice at the lunar south pole. J. Geophys. Res. 106, 23253–23266.

Ono, T. et al., 2009. Lunar radar sounder observations of subsurface layers under the nearside Maria of the Moon. Science 323 (5916), 909–912. doi:10.1126/science.1165988.

Ouyang, Z.Y. et al., 2010. Primary scientific results of Chang'E-1 lunar mission. Sci. China Ser. D 53, 1565–1581.

Paige, D.A., 2009. Diviner Observes Extreme Polar Temperatures. Diviner Lunar Radiometer Experiment. <http://www.diviner.ucla.edu/blog/?p=232>.

Paige, D.A. et al., 2010. The lunar reconnaissance orbiter diviner lunar radiometer experiment. Space Sci. Rev. 150 (1-4), 125–160. doi:10.1007/s11214-009-9529-2.

Price, S.D., Mizuno, D., 2003. Thermal profiles of the eclipsed Moon. Adv. Space Res. 31 (11), 2299–2304. doi:10.1016/S0273-1177(03)00531-3.

Schloerb, F.P., Muhleman, D.O., Berge, G.L., 1976. Lunar heat flow and regolith structure inferred from interferometric observations at a wavelength of 49.3 cm. Icarus 29, 329–341.

Sharpe, B.L., Schrunk, D.G., 2003. Malapert mountain: Gateway to the Moon. Adv. Space Res. 31, 2467–2472.

Shorthill, R.W., Saari, J.M., 1965. Nonuniform cooling of the eclipsed Moon: A listing of thirty prominent anomalies. Science 150, 210–212.

Siegfried, W.H., 1999. Lunar base development missions. Acta Astronaut. 44, 755–767.

Spudis, P.D. et al., 2010. Initial results for the north pole of the Moon from Mini-SAR, Chandrayaan-1 mission. Geophys. Res. Lett. 37, L06204.

Wang, X.D. et al., 2010. Acceleration of scattered solar wind protons at the polar terminator of the Moon: Results from Chang'E-1/SWIDs. Geophys. Res. Lett. 37, L07203. doi:10.1029/2010GL042891.

Wang, Z.Z., Li, Y., Jiang, J.S., Li, D.H., 2010a. Lunar surface dielectric constant, regolith thickness, and 3He abundance distributions retrieved from the microwave brightness temperatures of CE-1 Lunar Microwave Sounder. Sci. China Ser. D 53 (9), 1365–1378. doi:10.1007/s11430-010-4022.

Wang, Z.Z. et al., 2010b. Calibration and brightness temperature algorithm of CE-1 Lunar Microwave Sounder (CELMS). Sci. China Ser. D 53 (9), 1392–1406. doi:10.1007/s11430-010-4008.

Zhang, H.Y., Zhang, X.H., Yang, J.L., 2008. The analysis of affections to the cold space calibration source of ChangE-1 payload Microwave Detector. Adv. Space Res. 42, 350–357. doi:10.1016/j.asr.2007.04.010.

Zheng, Y.C., 2005. Development of Lunar Soil Stimulants and Characteristics of Microwave Radiation of Lunar Regolith. Ph.D. Thesis. Institute of Geochemistry, Chinese Academy of Sciences, Beijing. 150pp.

Zheng, Y.C., Ouyang, Z.Y., Li, C.L., Liu, J.Z., Zou, Y.L., 2008. China's Lunar Exploration Program: Present and future. Planet. Space Sci. 56 (7), 881–886. doi:10.1016/j.pss.2008.01.002.

Zheng, Y.C., Zou, Y.L. Chan, K.L., Tsang, K.T., Kong, B., Ouyang, Z.Y., 2010. Global brightness temperature of the Moon: Result from Chang'E-1 microwave radiometer. European Planetary Science Congress, vol. 5, EPSC2010-224.

Zhou, M.X., Zhou, J.J., Zhang, X., Wang, Fei., 2010. Inversion of microwave brightness temperature data for estimating lunar regolith thickness. Int. J. Appl. Electromag. 33, 1041–1048.